Density functional theory study on magnetically detecting positively charged nitrogen-vacancy center in diamond

Claire J. Meara*
School of Engineering, Newcastle University, Newcastle upon Tyne, NE1 7RU, United Kingdom
and Centre for Doctoral Training in Diamond Science and Technology, University of Warwick, Coventry, CV4 7AL, United Kingdom

Mark J. Rayson, Patrick R. Briddon, and Jonathan P. Goss
School of Engineering, Newcastle University, Newcastle upon Tyne, NE1 7RU, United Kingdom

(Received 8 November 2018; revised manuscript received 20 February 2019; published 10 September 2019)

A quantum-chemical study of the positive charge-state of the nitrogen-vacancy center in diamond is presented. Charge control of this promising qubit candidate is a focus of diamond quantum technology research, as currently charge stability relating to surfaces and nearby defects causes some difficulties for quantum applications. To demonstrate full charge control over the nitrogen vacancy, all three charge states should be identified and the processes that lead to charge state changes understood. However, experimental markers for the positive state remain elusive compared to the readily detectable zero-phonon lines of the neutral and negative. In this work we present predicted hyperfine and zero-field splitting tensors as clear signatures of the normally spinless NV^+ ($^1A_1$ ground state) by probing a long-lived spin-triplet excited-state ~0.7 eV above the NV^+ ground state. We find a relatively narrow excitation energy range of approximately 0.7–1.1 eV between excitation into an ^3E state and conversion into the neutral charge state. To provide insight into the thermal stability of the positive charge state, we have calculated binding and diffusion energies for both charged and uncharged systems. We predict, given that the activation energies are only weakly charge state dependent, all three charge states would diffuse in the 1600–1900 °C range, but the positive state has a significantly lower binding energy, suggesting that it will dissociate at temperatures around 1000 °C rather than migrate.

DOI: 10.1103/PhysRevB.100.104108

I. INTRODUCTION

The bond strength and relatively spin-free nature of the diamond lattice [1,2] provides a near ideal environment for stable single-photon sources [3]. Point defects have highly localized states, which can be manipulated, are stable at room temperature, and have long coherence times with intense optical signals [4]. Several defects have been extensively investigated for quantum applications, including those involving nickel and silicon [5,6] and, prominently, the nitrogen-vacancy (NV) complex [7]. The negatively charged NV center (NV^-) is especially promising for quantum technology due to low spin-orbit coupling [1] and an optically controllable spin triplet ground state [8], with applications in magnetometry [9], quantum registers [10], quantum information, and quantum computing [11]. Given its importance, its geometry, electronic structure, magnetic and optical signatures are well understood [12]. The neutral charge state, NV^0, is not directly of importance in quantum-technology applications, but it is also well understood [12]. Current NV research focuses on establishing full, manipulable charge control [13] as charge instability is a known issue with NV [14], affecting optical readout efficiency [9,13,15,16] and magnetic applications [14].

To establish charge control, the stability of each charge state must be established. NV^- and NV^0 are identifiable from strong 637 nm and 575 nm zero-phonon lines, distinctive phonon side bands, and ground spin states of $S = 1$ and $S = 1/2$, respectively [12]. However, the positive charge state (NV^+) currently lacks such clear optical or magnetic signatures; the removal of an electron from NV^0 is thought to result in a spin-singlet ground-state and small intra-band-gap transitions that are not optically active [17]. Due to the relative absence of direct experimental observation of NV^+, its comprehensive characterization has been hindered, limiting the understanding required for full NV charge control. Although reports of experimental identification are not unambiguous, NV^+ has been linked with a number of observations [14,15,17–19]. The evidence of NV^+ is either a byproduct of charge-control experiments [14,15,18,19] or the focus during attempts to increase T_2 [17]. Charge control experiments employ surface band bending to alter charge states, by either altering the diamond surface chemically [14], electrically [15], or both [18,19]. Band bending then raises or lowers the electron chemical potential past the $NV^{(0/+)}$ (donor) and $NV^{(-/0)}$ (acceptor) electrical transitions. One report describes full control across the three charge states [19], while others report that the $(-/0)$ level is directly observed, but another transition appears from NV^0 to an unknown dark state [14,15].

Reporting absence of fluorescence when Fermi levels are aligned to the theoretical donor level goes some way towards identifying NV^+, but it should be noted that there is a ~0.5 eV range of theoretical estimates [20–23] of the NV donor level used to support experimental observations. This renders the

*c.j.meara2@ncl.ac.uk

interpretation of the experimental data problematic, as it depends upon which of the theoretical estimates is deemed most reliable. Therefore we suggest more direct NV^+ detection methods are required for a confident assignment.

Although NV^+ is predicted to have a spin-singlet ground state, there are potentially excited spin-polarized configurations. Such excited-state configurations have been detected in other defects, including the $^5A_2$ excited state of V^0 [24] and the $^4A_2$ excited state of NV^0 [25], where electron paramagnetic resonance (EPR) experiments have successfully afforded both geometric and chemical fingerprints. In this study we show a ^3E excited state lies in the band gap, and present predicted magnetic signatures that provide a direct route to identification of NV^+. In addition, we present calculated binding and diffusion energies to provide insight into the thermal stability of this charge state.

II. METHOD

Density functional theory calculations have been performed using the AIMPRO [26] and FHI-AIMS [27] software packages. AIMPRO data have been obtained at both local density (LDA) [28] and generalized gradient (GGA) [29] levels, with pseudopotentials [30] used to obviate the explicit inclusion of the 1*s* core electrons. FHI-AIMS was performed at an all-electron level [27]. The Kohn-Sham functions are expanded in a basis of atom-centered Gaussian functions [31] of four widths with independent *s*, *p*, and *d* character, representing 40 functions per atom. A plane wave expansion of density and Kohn-Sham potential [26] was used to determine the matrix elements of the Hamiltonian, with a cutoff of at least 175 Ha, yielding well-converged total energies with respect to this parameter.

FHI-AIMS, all-electron calculations use the HSE06 [32,33], screened-exchange functional (SX) with a screening parameter of $\omega = 0.11$ bohr^{-1}. For the calculation of the Hamiltonian matrix and charge density a real-space grid discretization is employed [33]. Numeric atom-centered orbital basis is used comprised from a flexible radial component depending on the modeled element [27]. The use of two codes and different functionals has been adopted to provide evidence of the impact of functional on energetics [34].

A full many-body evaluation including multideterminant approaches to include configuration-interactions is beyond the scope of this study. Unlike the cases of NV^0 and NV^-, the many-body configurations we are most interested in are based upon different arrangements of electrons in different one-particle orbitals, and multiplet effects may be expected to be less important in this case.

NV^+ was modeled in a range of simple-cubic supercells based upon repeated conventional unit cells. The four sizes examined have side lengths of $2a_0$, $3a_0$, $4a_0$, and $5a_0$, containing 64, 216, 512, and 1000 atoms, respectively. The Brillouin zone was sampled using the Monkhorst-Pack scheme with a sampling density was $\leqslant 0.013$ Å^3.

In the examination of band structure, localized states resonant with the host bands are identified by examination of a Mulliken population. Bands for which the sums of the Mulliken populations over the atoms in the immediate vicinity of the vacancy are large are identified and their orbital character analyzed to facilitate comparison with the literature.

Donor and acceptor levels were estimated using the formation energy method [35,36], using Eq. (1).

$$E^f(X,q) = E_{\rm tot}(X,q) - \sum \mu_i + q\left(E_v^X + \mu_e\right) + \chi(X,q). \tag{1}$$

Here $E_{\rm tot}$ is the total energy of the defect in charge state q, μ_i, and μ_e are atomic and electronic chemical potentials, respectively, E_v^X is the energy of the valence band maximum, and χ is a correction term to take into account the periodic boundary condition [36–38]. The Madelung terms within χ for 1000, 512, 216, and 64 atom supercells were $0.21q^2$ eV, $0.26q^2$ eV, $0.35q^2$ eV, and $0.53q^2$ eV, respectively. The average electrostatic potential in the bulk regions of supercells containing the point defects varied by a few 10s of meV for 216 and 512 atom, meaning that the deviation of the valence-band top energy in these calculations from the pure-diamond case is of this order. Binding energies may also be obtained from the formation energies [38], and we use the convention that the binding energy is the energy released in the formation of the complex.

Migration barriers were calculated using the climbing nudged-elastic-band method [39,40] (NEB) using AIMPRO, 216-atom supercell and a minimum of nine images. Hyperfine tensor principal values and directions were determined as described previously [41,42], using AIMPRO within the GGA. The spin-spin contribution to a zero-field splitting (D tensor) was also calculated as described in Refs. [43,44].

III. RESULTS AND DISCUSSION

We start with the geometry and electronic structure of NV^+ in its ground state. As established for the neutral and negative charge states, we find NV^+ possesses C_{3v} symmetry [12]. One geometric measure of NV is the volume of the tetrahedron with vertices at the three carbon and one nitrogen atom neighboring the vacancy. We find the optimized structures (1000-atom supercells) have volumes monotonically increasing with increasingly positive charge state; the volume of NV^- measured 13.34 a.u.^{3} with a 0.7% increase to NV^0 and a 2.7% to NV^+. This reflects an outward relaxation of the structure as electrons are removed from a bonding combination of sp^3 orbitals on the three carbon atoms (see below).

It is instructive to view the electronic structure of NV^+ in the light of NV^0 and NV^-, arising from a_1 and e gap levels and an a_1-level resonant with the valence band [12,45]. The a_1 resonant state can be thought of as a bonding combination of the sp^3 orbital on the three undercoordinated carbon sites with the nitrogen lone-pair orbital. The a_1 gap state is dominated by the N lone pair (but in antibonding combination with the the three C radicals), and the e orbitals can be characterized by partially bonding combinations of the three carbon radicals with no contribution from the N. The makeup of these orbitals are depicted in Fig. 1, and those of NV^- agree with previous studies [12,45]. NV^0 has the one-electron configuration $a_1^2a_1^2e^1$ with a ^2E ground-state wave function, and the spin-triplet ground state of NV^- is the $^3A_2$ from $a_1^2a_1^2e^2$. For NV^+ we find, in agreement with previous work [14], that the e

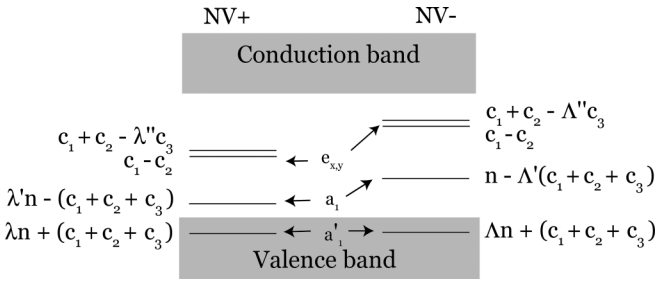

FIG. 1. Depiction of NV^+ and NV^- orbital make-up. c_1, c_2, and c_3 represent carbon sp^3 radicals and n is nitrogen lone-pair orbital. λ and Λ are used to indicate which site had more spin density for the NV^+ and NV^- orbitals respectively.

level in the band gap is empty, resulting in an $^1A_1$ many-body ground state. NV^+ orbitals differ in detail from those of NV^- in an increased localization on the nitrogen seen in the a_1 level in the gap (Fig. 1).

The NV^+ band-gap levels lie lower in energy and are closer together than found for NV^-. In particular, the energy difference from the band structure between fully occupied lowest-lying states and next available state for an electron excitation is much smaller in the NV^+ case (0.7 eV), compared to NV^- experimental values, which are approximately three times greater.

We next turn to an exploration of the excited many-body states. Several many-body excited states of NV^+ can be understood from one-electron configurations where electrons are promoted from one of the a_1 levels to the e level. Of these, there exist two paramagnetic configurations that present identifiable characteristics of NV^+, much as the $^5A_2$ V^0 [24] state reveals the neutral vacancy in EPR despite the ground state being EPR inactive. The excitation energies required to reach these states were obtained from the difference in the total energies of the optimized structures in each spin configuration, and are represented in Table I. Structural optimization of the excited states with SX could not be performed, so quoted energies correspond to the excited electronic state configurations using the optimized ground-state geometry. Including relaxation energies allows for an estimate of the relative energies of the excited states, as shown in parentheses in Table I. The $a_1^2 a_1^{\uparrow} e^{\uparrow}$ configuration (^3E) lies around $E(^1A_1) + 0.7$ eV, largely independent of the computational approach (Sec. II).

TABLE I. Energies (eV) of NV^+ many-body states relative to the $^1A_1$ ground state, comparing GGA and LDA pseudopotential values (AIMPRO) with and LDA and SX all-electron calculations (FHI-AIMS). AIMPRO calculations used 512-atom supercells and FHI-AIMS 64-atom supercells. The values in parentheses for FHI-AIMS calculations show estimated energies including relaxation as described in the text.

	AIMPRO		FHI-AIMS	
State	LDA	GGA	LDA	SX
^3E	0.8	0.6	0.7(0.6)	0.8(0.7)
^1E	1.0	0.9	0.8(0.7)	1.4(1.3)
$^3A_2$	1.9	1.5	2.0(1.7)	2.2(1.9)

An $a_1^2 a_1^0 e^{\uparrow\uparrow}$ configuration ($^3A_2$) appears to be more dependent upon the computational approach; the location is estimated to lie at $E(^1A_1) + 1.9$–2.0 eV in the LDA, around 1.5 eV in the GGA, and around 1.9–2.2 eV in SX. The relatively higher energy of this state in comparison to the ^3E is expected due to the process requiring the excitation of two electrons. There is also a ^1E state ($a_1^2 a_1^{\uparrow} e^{\downarrow}$), which is estimated to lie between the two spin-triplet states. Supercell size, sampling, and basis selection were all found to have no significant quantitative impact relative to the choice of functional, and all methods yielded the same sequence of states.

The relatively higher energy of the excited states obtained using the SX approach has to be considered carefully along with the estimated donor level. To further establish conditions under which NV^+ would be expected to be observable, we have estimated the electrical levels of NV.

Levels were examined using both AIMPRO and SX, considering a range of supercell sizes. Electrical transition points were found in the band gap, with donor and acceptor levels at $E_v + 0.9 \pm 0.1$ eV and $E_v + 1.9 \pm 0.1$ eV under LDA and GGA calculations (uncertainties reflect the different functionals), and $E_v + 1.3$ eV and $E_v + 2.2$ eV under SX based upon the same supercells used for the energies in Table I. The acceptor levels from both methods should be compared with the experimental value of $E_c - 2.58$ eV [46], and once the underestimate in the band gap is taken into account, both methods are in good agreement with observation. Where the electron chemical potential lies below the donor level the positive charge state will be the equilibrium form, so there exists a relatively narrow excitation range allowing EPR detection of the ^3E excited state that does not result in ionization (a margin of around a half an eV under the more quantitatively reliable SX estimate [47]). The location of the ^1E state relative to the donor level is less clear, with LDA and GGA simulations placing it below the donor level, and SX placing it very slightly above. However, the $^3A_2$ lies well above the ionization threshold independent of methodology, and is therefore much less likely to be useful in direct detection of NV^+.

Another possible route for direct identification of NV^+ may be an electronic transition between the $^1A_1$ ground state and a ^1E state arising from the $a_1^2 a_1^{\uparrow} e^{\downarrow}$ configuration, the predicted energy of which is also listed in Table I. Given the uncertainty in the ordering of the donor level and ^1E states highlighted above, we cannot be certain whether this state can be directly accessed optically. However, if the ^1E state can be accessed without ionizing, it is both dipole and spin allowed, and mechanistically analogous to the 1.945 eV transition of NV^-. To further characterize this potential optical transition, we calculated the optical absorption cross section from the dielectric function [48]. The optical spectrum exhibits an absorption peak at 0.9 eV, consistent with the many-body excitation energy (Table I), providing some hope that a direct optical signature of the center may be present. However, an electronic transition in the near infrared would not unambiguously provide evidence of the existence of NV^+, and alternative routes to identification would be highly desirable.

Given the potential for the direct observation of NV^+ in EPR, we have calculated the hyperfine interaction tensors for atoms in the vicinity of the defect, and in particular for the

TABLE II. Calculated anisotropic (A_{ani}) and isotropic (A_{iso}) components of the hyperfine interaction alongside principal values (MHz) for the nitrogen and three carbon atoms adjacent to the vacancy (C_1 Fig. 2) of the NV center. Values are shown for the spin polarized excited NV^+ states, NV^- spin-quartet excited state, and NV^0 spin-triplet ground state. Tensor directions are perpendicular and parallel to the trigonal [111] axis for nitrogen (Fig. 2). For carbon, angular deviations from the $[\bar{1}\bar{1}1]$ axis are in square brackets. ZFS, D, (GHz) are also included, calculated from Kohn-Sham functions at the R point in the Brillouin zone of 512 atom supercells, using AIMPRO within the GGA. All values are for 0% strain except for NV^+ ^3E, which was calculated for 0.1%. Values in parentheses indicate experimental values for NV^0 (Ref. [25]), NV^- (Ref. [49]) and D tensor values (Refs. [25,49,50]).

		Site	$\lvert A_\perp \rvert$	$\lvert A_\parallel \rvert$	$\lvert A_{iso} \rvert$	$\lvert A_{ani} \rvert$	D
		^{14}N	22.0	44.3	29.4	7.4	
NV^+	^3E	^{15}N	−28.9	−58.3	−38.7	−9.8	0.19
		^{13}C	54.9	125.2 [1°]	78.3	23.5	
		^{14}N	0.6	−5.5	−1.4	−2	
NV^+	$^3A_2$	^{15}N	−0.8	7.2	1.9	2.7	1.48
		^{13}C	75.6	179.5 [1°]	110.0	34.7	
		^{14}N	13.9	26.6	18.3	4.2	
NV^0	$^4A_2$	^{15}N	−18.3 (−23.8)	−35.0 (−35.7)	−23.8	−5.6	1.83 (1.69)
		^{13}C	77.4	153.7 [0°]	102.4	25.2	
		^{14}N	−2.0 (−2.7)	−1.6 (−2.14)	−1.9 (−2.51)	0.2 (0.19)	
NV^-	$^3A_2$	^{15}N	2.7 (3.65)	2.1 (3.03)	2.5 (3.44)	−0.2 (−0.21)	2.54 (2.87)
		^{13}C	111.4 (121.1)	198.0 (199.1) [1°]	140.2	28.9	

four atoms adjacent to the vacancy. The calculated principal values and directions of the hyperfine tensors at these sites are listed in Table II, based upon a [111]-orientated defect (Fig. 2). The carbon sites nearest the vacancy (C_1 Fig. 2) are not axial symmetric and therefore three principal values were calculated. The splitting of the perpendicular values were below the significance level of the calculation, up to only 0.3 MHz, therefore average values are presented and we expect the ^{13}C hyperfines to appear axial symmetric in EPR. We first review the principal values for the ^3E state of NV^+ ($a_1^2 a_1^{\uparrow} e^{\uparrow}$). In common with the ground states of NV^0 and NV^-, electron spin density is mostly associated with the carbon sp^3-hybrid radical orbitals. Consequently, the corresponding ^{13}C hyperfine interactions are relatively large. Since, in contrast to NV^0 and NV^-, the a_1 gap level associated with the N-related orbital is only partly occupied, there is significant spin density in the vicinity of the N atom, with a concomitantly large hyperfine interaction (Table II).

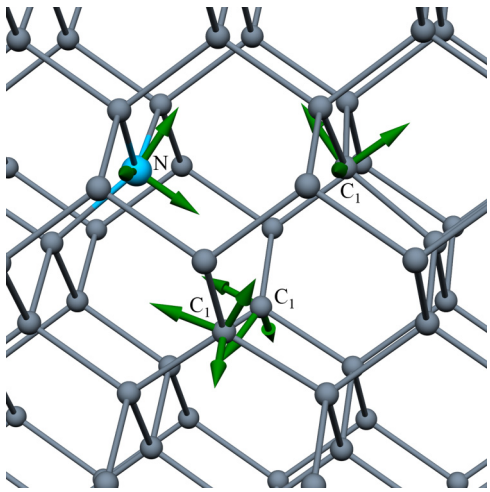

FIG. 2. Schematic of hyperfine tensors for the NV^+ (^3E) state. Equivalent C sites neighboring the vacancy are labeled C_1. Horizontal and vertical directions are $[\bar{1}\bar{1}0]$ and [001], respectively.

It instructive to compare the calculated NV^+ hyperfine interactions with those of the other charge states and experiment. The hyperfine tensors for the $S = 3/2$ excited state [25] of NV^0, can be viewed as arising from a one-electron configuration $a_1^2 a_1^{\uparrow} e^{\uparrow\uparrow}$. The experimental values for ^{15}N are $A_\perp = -24$ MHz and $A_\parallel = -36$ MHz [25], for which our calculated vales are in good agreement. The principal values are similar in magnitude and the same sign as those predicted for the ^3E state of NV^+, consistent with the underlying electronic configuration. This is in contrast to the calculated and experimental values for the $^3A_2$ state of NV^-, which, with the one-electron configuration $a_1^2 a_1^2 e^{\uparrow}$ ↑ has the hyperfine interaction arising from the polarization of the electron density in the vicinity of the N atom, and not from a partially occupied orbital. Both calculations and experiment indicate the magnitude and sign of the ^{15}N hyperfine principal values differ from NV^+. The overall agreement of our calculated values with the available experimental data for both neutral and negative charge states underlines the reliability of the predicted values for the case of NV^+.

Although the method adopted for this study does not eliminate errors arising from neglect of core polarization, such as explored previously for ^{13}C in the NV center [51], the significant differences between the calculated values for the ^3E state and those of other NV charge states is unlikely to be within error; given the quantitative reliability evidenced in comparative relevant experimental values for several impurity-related defects in diamond [41,42,52–55].

Before moving to another spin-Hamiltonian parameter, we briefly review the $^3A_2$ excited state of NV^+. The electron density in the vicinity of the N atom for the higher-energy $^3A_2$ excited state of NV^+ is comparable to the ground state of NV^+, since the lone-pair orbital is unoccupied and the

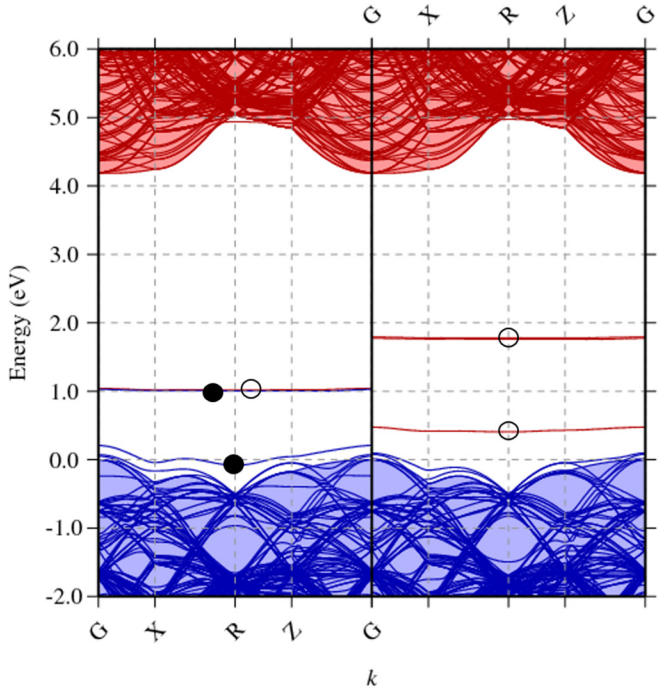

FIG. 3. Band structure in the vicinity of the band gap along high-symmetry directions of the first Brillouin zone NV^+ under 0.1%. The left and right panels represent spin-up and spin-down Kohn-Sham states, respectively. Blue (red) bands are occupied (empty), with the occupation of the a_1 and e-derived levels further indicated by filled and empty circles.

population of the e state matches that of NV^+. Thus, the small hyperfine principal values for ^{15}N and large values for the three ^{13}C sites are also readily understood.

To further illuminate the predicted magnetic signature of the excited states of NV^+ we have also estimated the zero-field splittings (ZFS). For comparison we also obtained D tensors for NV^- and NV^0 since there are experimental values for these cases [25,49]. We explored the impact of sampling, basis, and cell size, with NV^+ exhibiting a proportionally greater sensitivity to these parameters due to the involvement of an orbital with energy close to the valence band top [43], although in absolute terms the impact of parameter choice was similar for all cases. Values displayed were obtained using the electron states at the Brillouin-zone boundary (the R point), where the defect states are most distant in energy from the diamond bands (Fig. 3). Also visible in Fig. 3 is a splitting in the e level, deliberately introduced by application of a 0.1% uniaxial strain in order to allow us to selectively include the different components in the estimation of the ZFS. The values of D obtained whether the upper- or lower-energy component of the e state is used in estimation of the ZFS differ only very slightly, and we report the average of the values. The dipolar ZFS term can be expressed via the equations below [56,57].

$$\begin{aligned} \mathcal{H}_{\text{dip}} &= D + E \\ D &= \tfrac{3}{2} D_z \\ E &= \tfrac{1}{2}(D_x - D_y), \end{aligned} \tag{2}$$

where $\mathcal{H}_{\text{dip}}$ is the dominant spin-spin contribution to the spin Hamiltonian [56], D_z is the principal component of the D tensor ($D_\parallel$), and E indicates the rhombicity of a nontrigonal system [56,57]. The agreement with experiment is reasonable for both NV^- and NV^0, and we conclude that NV^+ will have a much smaller ZFS than the other charge states. A predicted value of D further facilitates identification of NV^+.

Considering the above discussion of the NV^+ electronic and hyperfine structure we discuss the feasibility of controlling NV^+, enabling readouts of certain spin states. First, the presence of NV^+ is expected to occur in materials where there is substitutional boron in the vicinity of NV^0; such substitutional boron would then act as an acceptor, thus creating NV^+. It has already been suggested the weak interaction NV^+ would have with its environment would make it a good candidate for quantum applications [17], but fine-tuned spin control as exhibited in NV^- is also necessary. For NV^+ there are two mechanisms that may be envisaged for the population of the ^3E state. For one, we propose optical pumping at energies above 0.9 eV and below the ionisation energy of 1.1–1.3 eV to directly promote from the $S = 0$ ground state to the ^1E excited state, which may then relax via an intersystem crossing to the ^3E state. The second mechanism is that in a transitory ionization process, capture of a hole by NV^0 can be into any of the many-body states that lie below the donor level, of which the calculations strongly support the paramagnetic ^3E state being one.

This is understood to be the mechanism by which the $^5A_2$ excite state of the neutral vacancy is observed [24]. The probability of an intersystem crossing mechanism can be estimated computationally [58], as has been performed for other charge states of the NV center [59]. However, given that there is at least one other mechanism by which the ^3E excited state may be experimentally populated we have not determined an estimate of the intersystem crossing probability for the positive charge state; this is something that will be of interest for a future study, especially in the context of potential spin control with this qubit, which would require experimental verification as shown for NV^- [12] or NV^0 [60].

We now turn to the binding and migration energetics. By comparing these two properties it can be determined whether, as T increases, NV is expected to migrate through the lattice as a unit or preferentially dissociate into its component parts. Binding energies (Table III) were calculated

TABLE III. Binding energies (eV) presented using GGA, LDA, and SX. All values involving charged species include the Madelung energy correction. Values in parentheses show the result when using the QMC formation energy [61] for V^0 (6.0 eV) rather than the DFT result.

Complex	Components	LDA	GGA	SX
NV^-	$N_S^0 + V^-$	4.3	3.9	4.3
NV^-	$N_S^- + V^0$	6.4 (5.3)	7.4 (7.0)	7.0 (5.8)
NV^0	$N_S^+ + V^-$	3.3	3.0	3.1
NV^0	$N_S^0 + V^0$	4.5 (3.5)	4.1 (3.6)	4.4 (3.2)
NV^+	$N_S^+ + V^0$	2.5 (1.4)	2.1 (1.7)	2.2 (1.1)

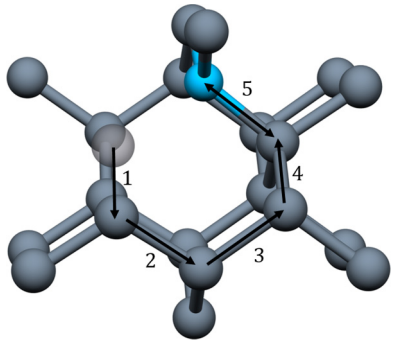

FIG. 4. A schematic of the NV diffusion pathway viewed along [110], with [001] vertical. The translucent sphere indicates the initial site of the vacancy and numbered arrows indicate its progression through four steps. Steps 1 and 4 are equivalent to each other, as are steps 2 and 3. Step 5 is the N exchanging places with the vacancy.

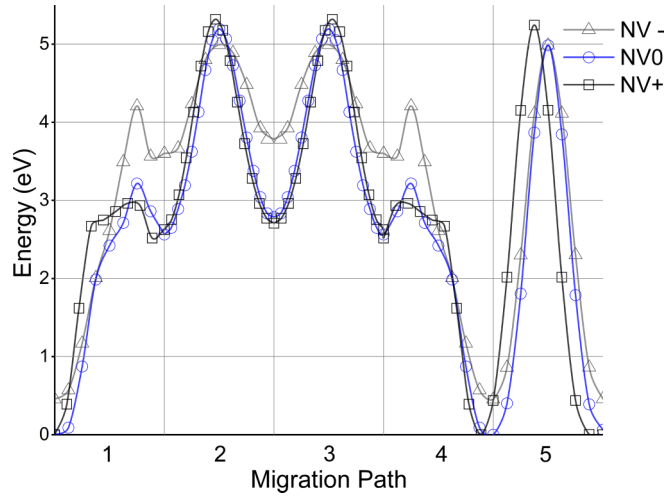

FIG. 5. NEB energy profiles for full diffusion processes as a function of NV charge state. The migration path is numbered as indicated in Fig. 4. Open shapes indicate energies of optimized images within the NEB structure. Solid lines included to guide the eye.

using GGA, LDA, and SX to provide insight into the impact of computational approach [34]. We noted that the ground state of the neutral vacancy, V^0, is a many-electron problem [61], so standard DFT simulations overestimate its formation energy. Therefore, we report binding energies based upon V^0 formation energy using DFT and the value of 6.0 eV from QMC simulations [61]. This also affords comparison with previous theoretical results [62].

The binding energies in Table III show different functionals yield values within around 0.2 eV. Our values also agree well with previous work [62] where the DFT value for V^0 was used. The data show NV^- and NV^0 preferentially dissociate into products involving V^-, but it is important to note that experimentally [63] it has been determined V^- undergoes a charge transformation to V^0 prior to migration, and V^0 moves with a barrier of 2.3 eV. In contrast to the known charge states, we find that NV^+ dissociates into N_S^+ and V^0, so this mobile species is immediately formed.

Diffusion of NV in all charge states is expected to follow in Fig. 4, as explored previously [64]. The barrier may either be the vacancy hopping between two carbon sites or the N hopping across the vacancy. Although the spin triplet is the ground state for NV^-, when the complex is in an intermediate structure during migration the ground state is the spin singlet. Thus, although we have calculated the barriers for both spin states of NV^-, we present the energetics for migration of the spin singlet, with the energies offset by the single-triplet splitting.

The minimum energy path profiles are shown in Fig. 5, with the rate-limiting steps and energies listed in Table IV. Interestingly, we find the barrier height only weakly depends upon charge state, although NV^+ appears less mobile than the others.

The estimated migration temperatures listed in Table IV are based upon Boltzmann statistics using $\nu \exp(-W/kT) = 1$ where ν, the attempt frequency, is taken to be the Γ-phonon frequency (10^{13} Hz), and W is the barrier height [64]. Assuming an uncertainty in the barrier height of ± 0.2 eV, the ranges of annealing temperatures overlap, and it is not possible to conclude with confidence the different charge states will migrate selectively based upon annealing conditions.

An alternative to the NV centers migrating as a complex, eventually being lost to a trap such as another defect (e.g., N_s) or a surface, is that the complexes dissociate into N_s and V. The dissociation barrier may be approximated as the sum of the binding energy and vacancy migration energy, since N_s is immobile relative to V. Taking the SX binding energies, and the migration barriers [63] for V^0 as 2.3 eV, respectively, the dissociation barriers can be computed, with the values listed in Table IV.

The energetic analysis of binding, diffusion, and dissociation suggest that the rate-limiting step for all charge states is the vacancy hopping between carbon sites, agreeing with previous findings [22,64]. It also presents a significant difference between the charge states: NV^+ is expected to dissociate before it migrates opposed to NV^0 and NV^-. For the neutral and negative cases the migration barrier is 5.0 eV and 5.2 eV respectively which are both lower than the calculated dissociation barriers (7.1 and 5.5 eV). For the positive case, the diffusion barrier of 5.3 eV is significantly greater than the dissociation barrier at 3.4–4.5 eV, depending upon the value taken for the V^0 formation energy. This implies that NV^+ should anneal out temperatures hundreds of degrees lower than either NV^0 or NV^-, releasing vacancies in the process.

TABLE IV. Rate-limiting steps and their associated diffusion energies (eV) for three charge states of NV. Estimated diffusion temperatures (°C) are determined as described in the text. Also listed are the dissociation energies (eV) based upon the sum of the binding energies calculated (using SX and the corrected V^0 formation energy) and the neutral vacancy diffusion barrier (2.3 eV).

Defect	Step	Diff. barrier	Temp.	Diss. barrier
NV^-	2 & 3	5.0	1590–1740	7.1
NV^0	2 & 3	5.2	1670–1820	5.5
NV^+	2 & 3	5.3	1700–1860	3.3

In fact NV^+ in samples could be dissociating at temperatures from 1000−1500 °C, which should be of interest to those attempting to fabricate samples containing NV^+. Currently samples are annealed between 600−1000 °C for NV center creation [65], where 800 °C is used commonly as standard [15,18,19], but temperatures even above 1000 °C are stated to increase efficiency of NV production [66] as well as higher temperatures being used as a method to improve coherence times 950 °C [17]. In such works where NV^+ is crucial to the application and temperatures nearing 1000 °C are currently used [17] use of lower temperatures may be advised.

IV. CONCLUSIONS

This work presents a theoretical analysis of positively charged NV in diamond, providing predictions of experimental signatures for the unambiguous identification of this system. In particular, magnetic characteristics were calculated for a low-lying ^3E excited state. It is important to note that EPR characterization under illumination has been successfully demonstrated in this way for the $^5A_2$ excited state of V^0 in diamond [24] and the $^4A_2$ excited state of NV^0 [25]. This makes the hyperfine tensors of the ^3E state of NV^+ a highly promising route for similar NV^+ identification, with the data provided here showing the hyperfine interactions to be significantly different from those of the other charge states.

The ^3E is predicted to be the lowest-lying configuration at 0.7 eV above the ground state indicating infrared excitation would be required for experiment. Being the lowest-lying spin-triplet state, there are no spin-allowed dipole relaxation mechanisms, suggesting the ^3E excited state would be long lived. The excited spin state lies below the ionization threshold, with the donor level predicted to lie 1.1–1.3 eV above the valence band maximum. Hence a 0.7–1.1 eV excitation energy range is available before NV^+ is ionized. This also admits the possibility of an electronic transition between the $^1A_1$ ground state and a ^1E excited state around 1.3 eV higher in energy based upon the SX calculations. The relative proximity of the excited spin-singlet state to the predicted ionization energy renders the role of this state less certain than the presence of an EPR active excited state.

Calculated hyperfine tensors parallel and perpendicular to ⟨111⟩ for NV^+ are more than an order of magnitude greater and the opposite sign to those of NV^-. Furthermore, because the spin density of NV^+ involves a partially occupied sp^3 orbital centered on the N site, the hyperfine interactions in NV^+ are also more anisotropic. In addition the zero field splitting D tensor for NV^+ is predicted to be an order of magnitude smaller than that of NV^-. The combination of these significant differences are key to experimental NV^+ identification.

A further distinction between NV^+ and the other charge states has been identified in the binding and migration energetics. We find that although the generally accepted migration mechanism for NV yields similar activation energies for all charge states, the significantly lower binding energy of NV^+ means it will dissociate rather than diffuse as a unit. An estimate based upon the low temperature limit for the binding energy and Boltzmann statistics, suggests NV^+ should dissociate into V^0 and N_s^+ at around 1000 °C, much lower than the diffusion temperatures of NV^0 and NV^-.

Up to now experimental studies have largely relied upon an absence of an optical signature to infer the presence of NV^+. Our work shows the route to clear, direct identification through magnetic probing under illumination, similar to identification of related defects in diamond [24,25].

ACKNOWLEDGMENTS

This research made use of the Rocket High Performance Computing service at Newcastle University. Many thanks to Phil Diggle and Ben Green at Warwick University for inspiration and discussions throughout. Also, much thanks to funding received from the EPSRC Centre for Doctoral Training in Diamond Science & Technology Grant No. EP/L015315/1.

[1] T. D. Ladd, F. Jelezko, R. Laflamme, Y. Nakamura, C. Monroe, and J. L. O'Brien, Nature (London) **464**, 45 (2010).

[2] G. Balasubramanian, P. Neumann, D. Twitchen, M. Markham, R. Kolesov, N. Mizuochi, J. Isoya, J. Achard, J. Beck, J. Tissler, V. Jacques, P. R. Hemmer, F. Jelezko, and J. Wrachtrup, Nature Mater. **8**, 383 (2009).

[3] A. Batalov, C. Zierl, T. Gaebel, P. Neumann, I. Chan, G. Balasubramanian, P. R. Hemmer, F. Jelezko, and J. Wrachtrup, Phys. Rev. Lett. **100**, 077401 (2008).

[4] B. C. Rose, C. D. Weis, A. M. Tyryshkin, T. Schenkel, and S. A. Lyon, Diam. Relat. Mater. **72**, 32 (2017).

[5] D. Steinmetz, E. Neu, C. Hepp, R. Albrecht, W. Bolse, J. Meijer, D. Rogalla, and C. Becher, Appl. Phys. B **102**, 451 (2011).

[6] D. D. Sukachev, A. Sipahigil, C. T. Nguyen, M. K. Bhaskar, R. E. Evans, F. Jelezko, and M. D. Lukin, Phys. Rev. Lett. **119**, 223602 (2017).

[7] N. H. Wan, B. J. Shields, D. Kim, S. Mouradian, B. Lienhard, M. Walsh, H. Bakhru, T. Schröder, and D. Englund, Nano Lett. **18**, 2787 (2018).

[8] R. Hubbard, Y. B. Ovchinnikov, J. Cheung, N. Fletcher, and R. Murray, J. Mod. Opt. **54**, 441 (2007).

[9] L. Rondin, J.-P. Tetienne, T. Hingant, J.-F. Roch, P. Maletinsky, and V. Jacques, Rep. Prog. Phys. **77**, 056503 (2014).

[10] M. V. G. Dutt, L. Childress, L. Jiang, E. Togan, J. Maze, F. Jelezko, A. S. Zibrov, P. R. Hemmer, and M. D. Lukin, Science **316**, 1312 (2007).

[11] P. C. Humphreys, N. Kalb, J. P. J. Morits, R. N. Schouten, R. F. L. Vermeulen, D. J. Twitchen, M. Markham, and R. Hanson, Nature (London) **558**, 268 (2018).

[12] M. W. Doherty, N. B. Manson, P. Delaney, F. Jelezko, J. Wrachtrup, and L. C. Hollenberg, Phys. Rep. **528**, 1 (2013).

[13] L. Hacquebard and L. Childress, Phys. Rev. A **97**, 063408 (2018).

[14] M. V. Hauf, B. Grotz, B. Naydenov, M. Dankerl, S. Pezzagna, J. Meijer, F. Jelezko, J. Wrachtrup, M. Stutzmann, F. Reinhard, and J. A. Garrido, Phys. Rev. B **83**, 081304(R) (2011).

[15] M. V. Hauf, P. Simon, N. Aslam, M. Pfender, P. Neumann, S. Pezzagna, J. Meijer, J. Wrachtrup, M. Stutzmann, F. Reinhard *et al.*, Nano Lett. **14**, 2359 (2014).
[16] O. Faklaris, V. Joshi, T. Irinopoulou, P. Tauc, M. Sennour, H. Girard, C. Gesset, J.-C. Arnault, A. Thorel, and J.-P. Boudou, ACS Nano **3**, 3955 (2009).
[17] M. Pfender, N. Aslam, P. Simon, D. Antonov, G. Thiering, S. Burk, F. Fávaro de Oliveira, A. Denisenko, H. Fedder, J. Meijer, J. A. Garrido, A. Gali, T. Teraji, J. Isoya, M. W. Doherty, A. Alkauskas, A. Gallo, A. Grüneis, P. Neumann, and J. Wrachtrup, Nano Lett. **17**, 5931 (2017).
[18] B. Grotz, M. V. Hauf, M. Dankerl, B. Naydenov, S. Pezzagna, J. Meijer, F. Jelezko, J. Wrachtrup, M. Stutzmann, F. Reinhard, and J. A. Garrido, Nature Commun. **3**, 729 (2012).
[19] C. Schreyvogel, V. Polyakov, R. Wunderlich, J. Meijer, and C. E. Nebel, Sci. Rep. **5**, 12160 (2015).
[20] J. P. Goss, P. R. Briddon, M. J. Rayson, S. J. Sque, and R. Jones, Phys. Rev. B **72**, 035214 (2005).
[21] J. R. Weber, W. F. Koehl, J. B. Varley, A. Janotti, B. B. Buckley, C. G. Van de Walle, and D. D. Awschalom, Proc. Natl. Acad. Sci. USA **107**, 8513 (2010).
[22] P. Deák, B. Aradi, M. Kaviani, T. Frauenheim, and A. Gali, Phys. Rev. B **89**, 075203 (2014).
[23] E. Londero, E. Bourgeois, M. Nesladek, and A. Gali, Phys. Rev. B **97**, 241202(R) (2018).
[24] J. A. Van Wyk, O. D. Tucker, M. E. Newton, J. M. Baker, G. S. Woods, and P. Spear, Phys. Rev. B **52**, 12657 (1995).
[25] S. Felton, A. M. Edmonds, M. E. Newton, P. M. Martineau, D. Fisher, and D. J. Twitchen, Phys. Rev. B **77**, 081201(R) (2008).
[26] M. J. Rayson and P. R. Briddon, Phys. Rev. B **80**, 205104 (2009).
[27] V. Blum, R. Gehrke, F. Hanke, P. Havu, V. Havu, X. Ren, K. Reuter, and M. Scheffler, Comput. Phys. Commun. **180**, 2175 (2009).
[28] J. P. Perdew and Y. Wang, Phys. Rev. B **45**, 13244 (1992).
[29] J. P. Perdew, K. Burke, and M. Ernzerhof, Phys. Rev. Lett. **77**, 3865 (1996).
[30] C. Hartwigsen, S. Gœdecker, and J. Hutter, Phys. Rev. B **58**, 3641 (1998).
[31] J. P. Goss, M. J. Shaw, and P. R. Briddon, *Theory of Defects in Semiconductors*, Vol. 104 (Springer, Berlin, Heidelberg, 2007), pp. 69–94.
[32] J. Heyd, J. E. Peralta, G. E. Scuseria, and R. L. Martin, J. Chem. Phys. **123**, 174101 (2005).
[33] V. Havu, V. Blum, P. Havu, and M. Scheffler, J. Comput. Phys. **228**, 8367 (2009).
[34] C. Stampfl, W. Mannstadt, R. Asahi, and A. J. Freeman, Phys. Rev. B **63**, 155106 (2001).
[35] J. P. Goss, P. R. Briddon, R. Jones, and S. Sque, Diam. Relat. Mater. **13**, 684 (2004).
[36] S. B. Zhang and J. E. Northrup, Phys. Rev. Lett. **67**, 2339 (1991).
[37] M. Leslie and N. J. Gillan, J. Phys. C: Solid State Phys. **18**, 973 (1985).
[38] J. P. Goss and P. R. Briddon, Phys. Rev. B **77**, 035211 (2008).
[39] G. Henkelman, B. P. Uberuaga, and H. Jónsson, J. Chem. Phys. **113**, 9901 (2000).
[40] G. Henkelman and H. Jónsson, J. Chem. Phys. **113**, 9978 (2000).
[41] J. P. Goss, P. R. Briddon, and M. J. Shaw, Phys. Rev. B **76**, 075204 (2007).
[42] M. J. Shaw, P. R. Briddon, J. P. Goss, M. J. Rayson, A. Kerridge, A. H. Harker, and A. M. Stoneham, Phys. Rev. Lett. **95**, 105502 (2005).
[43] M. J. Rayson and P. R. Briddon, Phys. Rev. B **77**, 035119 (2008).
[44] M. J. Rayson, J. P. Goss, and P. R. Briddon, Physica B: Cond. Mat. **340–342**, 673 (2003).
[45] A. Gali, M. Fyta, and E. Kaxiras, Phys. Rev. B **77**, 155206 (2008).
[46] J. W. Steeds, S. J. Charles, J. Davies, and I. Griffin, Diam. Relat. Mater. **9**, 397 (2000).
[47] P. J. Hasnip, K. Refson, M. I. J. Probert, J. R. Yates, S. J. Clark, and C. J. Pickard, Philos. Trans. R. Soc., A **372**, 20130270 (2014).
[48] C. J. Fall, A. T. Blumenau, R. Jones, P. R. Briddon, T. Frauenheim, A. Gutiérrez-Sosa, U. Bangert, A. E. Mora, J. W. Steeds, and J. E. Butler, Phys. Rev. B **65**, 205206 (2002).
[49] S. Felton, A. M. Edmonds, M. E. Newton, P. M. Martineau, D. Fisher, D. J. Twitchen, and J. M. Baker, Phys. Rev. B **79**, 075203 (2009).
[50] C. A. J. Ammerlaan and Landolt-Bórnstein, *Numerical Data and Functional Relationships in Science and Technology* (Springer, Berlin, 1989).
[51] K. Szász, T. Hornos, M. Marsman, and A. Gali, Phys. Rev. B **88**, 075202 (2013).
[52] K. M. Etmimi, M. E. Ahmed, P. R. Briddon, J. P. Goss, and A. M. Gsiea, Phys. Rev. B **79**, 205207 (2009).
[53] C. V. Peaker, M. K. Atumi, J. P. Goss, P. R. Briddon, A. B. Horsfall, M. J. Rayson, and R. Jones, Diam. Relat. Mater. **70**, 118 (2016).
[54] J. M. Baker, J. A. van Wyk, J. P. Goss, and P. R. Briddon, Phys. Rev. B **78**, 235203 (2008).
[55] U. F. S. D'Haenens-Johansson, A. M. Edmonds, M. E. Newton, J. P. Goss, P. R. Briddon, J. M. Baker, P. M. Martineau, R. U. A. Khan, D. J. Twitchen, and S. D. Williams, Phys. Rev. B **82**, 155205 (2010).
[56] C. B. Hartland, Ph.D. thesis, University of Warwick, 2014.
[57] A. Abragam and B. Bleaney, *Electron Paramagnetic Resonance of Transition Ions* (Oxford University Press, Oxford, 2012), p. 152.
[58] G. Thiering and A. Gali, Phys. Rev. B **96**, 081115(R) (2017).
[59] G. Thiering and A. Gali, Phys. Rev. B **98**, 085207 (2018).
[60] A. Gali, Phys. Rev. B **79**, 235210 (2009).
[61] R. Q. Hood, P. R. C. Kent, R. J. Needs, and P. R. Briddon, Phys. Rev. Lett. **91**, 076403 (2003).
[62] T. L. Petrenko and V. P. Bryksa, J. Phys.: Condens. Matter **29**, 325506 (2017).
[63] G. Davies, S. C. Lawson, A. T. Collins, A. Mainwood, and S. J. Sharp, Phys. Rev. B **46**, 13157 (1992).
[64] H. Pinto, R. Jones, D. W. Palmer, J. P. Goss, P. R. Briddon, and S. Öberg, Phys. Status Solidi A **209**, 1765 (2012).
[65] C. Santori, P. E. Barclay, K.-M. C. Fu, and R. G. Beausoleil, Phys. Rev. B **79**, 125313 (2009).
[66] V. M. Acosta, E. Bauch, M. P. Ledbetter, C. Santori, K.-M. C. Fu, P. E. Barclay, R. G. Beausoleil, H. Linget, J. F. Roch, F. Treussart *et al.*, Phys. Rev. B **80**, 115202 (2009).